Mathematical Biosciences 381 (2025) 109381

Contents lists available at ScienceDirect

Mathematical Biosciences

journal homepage: www.elsevier.com/locate/mbs

Original research article

Dynamics of phase tumbling and the reentrainment of circadian oscillators

Guangyuan Liao [a], Casey O. Diekman [b,*], Amitabha Bose [b]

[a] Key Laboratory of Intelligent Analysis and Decision on Complex Systems, School of Science, Chongqing University of Posts and Telecommunications, Chongwen Road, Nan'an, 400065, Chongqing, China

[b] Department of Mathematical Sciences, New Jersey Institute of Technology, Newark, NJ 07102, United States of America

ARTICLE INFO

Dataset link: https://github.com/daybrown/Phase-tumbling-project/

Keywords:
Circadian rhythms
Entrainment
Phase tumbling
Iterated map

ABSTRACT

Circadian clocks are comprised of networks of cellular oscillators that synchronize to produce endogenous daily rhythms in gene expression and protein abundance. These clocks have evolved to align the physiology and behavior of organisms to the 24-h environmental cycles arising from Earth's rotation. Rapid travel across time zones causes misalignment between an organism's circadian rhythms and its environment, leading to sleep problems and other jet lag symptoms until the circadian system entrains to the external cycles of the new time zone. Experimental and modeling work has shown that phase tumbling, defined as desynchronizing networks of circadian oscillators prior to an abrupt phase shift of the light-dark cycle, can speed up the process of reentrainment. Here, we use a mathematical model of circadian oscillators and 2-D entrainment maps to analyze the conditions under which phase tumbling has a positive, neutral, or negative effect on reentrainment time. We find that whether or not phase tumbling is beneficial depends on the size of the external phase shift and the location of the perturbed oscillator with respect to the fixed points and invariant manifolds of the entrainment map.

1. Introduction

Circadian rhythms are endogenous biological oscillations with an intrinsic period of nearly 24 h. The circadian clock entrains to the external light-dark cycle and other 24-h periodic signals in the environment conferred by Earth's rotation. Circadian clocks are an evolutionary adaptation to these daily environmental cycles that align the physiology and behavior of an organism to appropriate times of the day. Robust circadian rhythms enable an organism to anticipate recurring events such as sunrise, sunset, and meal times. The circadian timekeeping system is also flexible enough to adjust to seasonal changes in daylength. However, modern society presents challenges to the circadian system, such as night shift work and long-distance transmeridian air travel, for which the clock did not evolve to handle [1].

An abrupt shift in the phase of the light-dark cycle, as occurs when switching from day shift to night shift or rapidly traveling across time zones, disrupts the alignment between circadian rhythms and environmental cycles. This misalignment leads to a variety of symptoms – including fatigue, insomnia, gastrointestinal disturbances, and impaired cognitive performance – that persist until the circadian clock entrains to the external cycles of the new work schedule or time zone. Treatments and strategies to speed up the reentrainment process are needed to reduce the duration of these symptoms [2]. Recently, researchers have proposed that perturbing the circadian clock shortly before traveling, or before switching shifts, can reduce the amount of time it takes the clock to reentrain [3–6]. In this paper, we use mathematical modeling and dynamical systems analysis tools to explore when and how such perturbations can aid reentrainment.

The central circadian clock in mammals, the suprachiasmatic nucleus (SCN), is a network of about 20,000 neurons located in the hypothalamus. The SCN is capable of generating self-sustained circadian oscillations in the absence of external inputs. These oscillations entrain to external light-dark cycles through the retinohypothalamic tract, a direct connection between the SCN and intrinsically photosensitive retinal ganglion cells [7]. Individual SCN neurons can also generate self-sustained circadian oscillations even when isolated from the network. The core intracellular timekeeping mechanism is a transcriptional-translational negative feedback loop in which the transcription of certain clock genes are inhibited by their own protein products, leading to ~24-h rhythms in gene expression and protein abundance. Vasoactive intestinal peptide (VIP) is a prominent intercellular signaling molecule within the SCN that plays a major role in synchronizing these rhythms across SCN neurons [8]. Unexpectedly, An et al. [3] found that brief exogenous application of VIP to SCN brain slices in vitro can desynchronize SCN neurons, leading to a reduction in gene expression rhythm amplitude at the population level.

* Corresponding author.
E-mail addresses: liaogy@cqupt.edu.cn (G. Liao), diekman@njit.edu (C.O. Diekman), bose@njit.edu (A. Bose).

https://doi.org/10.1016/j.mbs.2025.109381

Available online 8 February 2025

Based on previous studies associating lower-amplitude oscillations with enhanced entrainment properties [9–17]. An et al. hypothesized that VIP-induced desynchrony could accelerate reentrainment of SCN tissue rhythms to phase shifts in environmental cycles. To test this hypothesis, An et al. maintained SCN brain slices under a 12-h:12-h warm:cool cycle (8:00 PM warm, 8:00 AM cool) for 13 days before treating the slice with either VIP or vehicle (artificial cerebral spinal fluid) at 4:00 PM. Eleven hours later, the VIP- and vehicle-treated slices were subjected to a 10-h advance of the warm:cool cycle. Gene expression rhythms in the VIP-treated slices entrained to the new temperature cycle within 5 days on average, compared to nearly 10 days for the vehicle-treated slices.

An et al. also showed that VIP pretreatment in vivo can speed up reentrainment to a shift in the light cycle. In these experiments, mice were implanted with cannulae directed at the SCN and kept under a 12-h:12-h light:dark cycle (7:00 AM lights on, 7:00 PM lights off) for 7 days before receiving VIP or vehicle at 10:00 AM. The lights were turned off after the injection and then turned back on at 11:00 PM, resulting in an 8-h advance of the light schedule. The locomotor rhythms of VIP-treated animals entrained to the phase-shifted light schedule approximately 3 days faster than those of vehicle-treated animals.

To explain these findings, An et al. proposed that VIP pretreatment accelerates entrainment through a "phase tumbling" mechanism analogous to the "run and tumble" pattern of bacterial chemotaxis. In this paradigm, VIP application causes transient desynchrony due to heterogeneous responses across the population—the phases of individual SCN cells are affected by VIP stimulation to varying degrees [4]. Some of these "tumbled" cellular phases happen to align well with the phase of the new light-dark cycle. These cells "run" towards the new cycle, and speed entrainment of the population overall by communicating their proper phase through intercellular coupling.

Roberts et al. [5] have observed a similar phenomenon with circadian clock neurons in the fruit fly *Drosophila*. Unlike the mammalian brain, the fly brain responds directly to light in vitro, enabling Roberts et al. to study how clock gene expression rhythms are affected by light stimuli. They found that a light pulse transiently desynchronizes fly clock neurons, and that once cells resynchronize following the light pulse they exhibit greater synchrony and stronger rhythms than before the pulse.

These studies provide experimental evidence that desynchronizing networks of circadian oscillators prior to an abrupt phase shift of the light-dark (LD) cycle can speed up the process of entrainment. In this paper, we use a mathematical model of the *Drosophila* molecular clock [18] to analyze the dynamics of phase tumbling and determine the conditions under which it has a positive, neutral, or negative effect on reentrainment time. To do so, we consider a pair of mutually coupled oscillators that receive periodic, 24-h light-dark forcing. A stable, limit cycle solution exists for this model in which the oscillators are synchronized and entrained to the LD-cycle. Starting from this entrained limit cycle solution of the forced system, we systematically consider a set of phase tumbled (de-synchronized) initial conditions across a range of LD phases. We find that after a change of LD phase, only in some circumstances does phase tumbling speed up reentrainment relative to leaving the oscillators synchronized. In other cases, phase tumbling is either neutral or negatively impacts reentrainment times. To quantify and explain our findings, we use both direct simulations of systems of ordinary differential equations (ODEs) as well as discrete entrainment maps [19–23]. The entrainment map is two-dimensional and its fixed points correspond to entrained solutions. We show how the stable and unstable manifolds of these fixed points arrange the dynamics and provide insight into the circumstances and reasons why phase tumbling may or may not be beneficial. We also extend our model to the case of three coupled oscillators to show how to use the two-oscillator results to make predictions about the larger network. The results for the larger network also support the hypothesis that phase tumbling, in and of itself, is only beneficial for certain LD phase shifts.

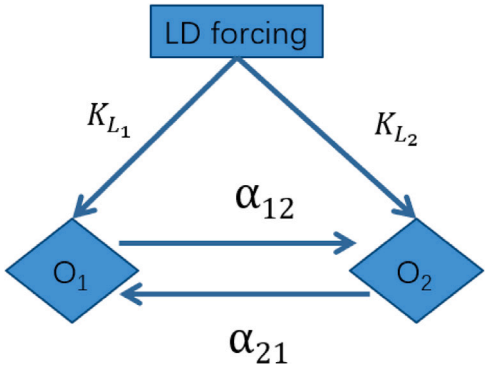

Fig. 1. Schematic of model network. Both oscillators O_1 and O_2 receive light input where K_{L_1} and K_{L_2} represent the forcing strength of the 24-h LD input. The oscillators are mutually coupled with strengths α_{12} and α_{21}.

2. Models and methods

We use the Novák–Tyson (NT) model [18] for the molecular circadian clock in the fruit fly *Drosophila melanogaster*. The model consists of two state variables, M and P, which represent mRNA and protein concentrations, respectively. Equations that govern these variables are:

$$\begin{aligned}\frac{dP}{dt} &= v_p M - k_f h(P) - k_D P - k_L f(t) P \\ \frac{dM}{dt} &= v_m g(P) - k_m M\end{aligned} \tag{1}$$

where $g(P) = 1/\left(1+P^4\right)$ and $h(P) = P/\left(0.1+P+2P^2\right)$. The model exhibits oscillations with a period of nearly 24 h in the absence of light-dark forcing. The dynamics of P are faster than M, at least for part of their excursion through phase space. In *Drosophila*, protein degradation occurs during darkness, but light increases this degradation. Thus, k_D represents the degradation rate during darkness, and k_L represents the additional degradation rate due to light. The parameter k_f reflects the strength of positive feedback that results from dimerization protecting the protein from degradation [18,24]. The parameters v_p, v_m, and k_m are rate constants for translation, transcription, and degradation of mRNA, respectively. The term $f(t)$ is a periodic square-wave function representing the light-dark (LD) forcing that equals 1 when lights are on and 0 when lights are off. For convenience, we assume a 12:12 photoperiod, though other cases may be considered without difficulty.

2.1. The coupled Novak-Tyson model

We consider two identical NT oscillators that are mutually coupled. Fig. 1 shows a schematic of the basic network structure. The model consists of an externally prescribed LD forcing which has direct input of strength k_{L_i} to each oscillator. Each NT oscillators is coupled to the other with strength α_{ij} indicating the direction from oscillator i to j. Later in the Results section we will also consider the generalization to more oscillators.

The equations that describe the dynamics of the coupled model are:

$$\begin{aligned}\frac{dP_1}{dt} &= v_p M_1 - k_f h\left(P_1\right) - k_D P_1 - k_{L_1} f(t) P_1 \\ \frac{dM_1}{dt} &= v_m g\left(P_1\right) - k_m M_1 + \alpha_{21} M_2 g\left(P_1\right) \\ \frac{dP_2}{dt} &= v_p M_2 - k_f h\left(P_2\right) - k_D P_2 - k_{L_2} f(t) P_2 \\ \frac{dM_2}{dt} &= v_m g\left(P_2\right) - k_m M_2 + \alpha_{12} M_1 g\left(P_2\right).\end{aligned} \tag{2}$$

The parameters α_{12} and α_{21} denote the coupling strength. In previous work [23], we have studied the strictly hierarchical network that results from setting $\alpha_{21} = 0, \alpha_{12} > 0$, and $k_{L_1} > 0, k_{L_2} = 0$. Now we extend that study in the context of phase tumbling to the fully coupled model for which α_{12} and α_{21}, k_{L_1} and k_{L_2} are all positive. The specific parameter values and their units are presented in Table 1.

Table 1
Model parameters. As in [18], C_p and C_m represent characteristic concentrations for protein (P) and mRNA (M), respectively.

Parameter	Value	Units
k_D	0.105	h^{-1}
k_{L_1}, k_{L_2}	0.105	h^{-1}
k_f	2.1	h^{-1}
k_m	0.105	h^{-1}
v_p	2.1	$C_p C_m^{-1} h^{-1}$
v_m	0.105	$C_p C_m h^{-1}$
α_{12}, α_{21}	0 or 0.0945	$C_p C_m h^{-1}$

2.2. Methods for determining reentrainment times

To determine reentrainment times, we first describe the LD-entrained periodic solutions to which phase-tumbled solutions will entrain. Consider the uncoupled model when the parameters $\alpha_{12} = \alpha_{21} = 0$. We and others have shown that the NT model [18] can entrain to a 24-h LD forcing. Fig. 2(a) shows the P-M phase plane as a projection onto which the separate lights on (black-nullcline) and lights off (blue-nullcline) phase planes are jointly shown. Since the two oscillators are identical, the LD-entrained solution represents the uncoupled limit cycle for both oscillator 1 and 2, respectively O_1 and O_2. Note that we will often separately refer to the LD-entrained limit cycle for O_1 and O_2. This refers to the projection of the LD-entrained solution onto the appropriate P-M phase space. Red portions of the trajectory indicate when the lights are on, and black when lights are off. Hourly markings are placed in green circles along the trajectory. Phase plane analysis is most typically used in 2-dimensional systems by using the nullclines to visualize fixed points and directions of flow. Here we extend that analysis by understanding how the nullclines and limit cycles change when lights are on or off, as well as a function of the different types of coupling. In Fig. 2(a), the two different P-nullclines correspond to when the lights are on or off and can be found by setting the right-hand side of the first equation in (2) equal to zero with different values of the forcing $f(t)$. Similarly, the M-nullclines is obtained by setting the right hand side of the second equation of (2) to zero with $\alpha_{21} = 0$. The intersection of the M-nullcline with either of the P-nullclines occurs along the middle branch of the latter and is unstable, and the projection of the stable periodic limit cycle surrounds it. Panel (b) shows the associated time courses of all four variables where different pairs overlap. Panels (c) and (d) correspond to the projected phase planes and trajectories in the uni-directional case when $\alpha_{12} > 0$ and $\alpha_{21} = 0$. Note here that the projected limit cycle of O_1 is identical to that in panel (a), while that of O_2 now has larger amplitude (also shown in panel (d) time courses). There are now three M-nullclines shown: the original one from panel (a) as well as two others labeled min (max) M-nullcline. The latter two correspond to the M-nullcline that occurs when $g(P_1)$ is at its min (max) which shifts the M-nullcline to the right. Panels (e) and (f) show the projected limit cycles and time courses when $\alpha_{12} = \alpha_{21} > 0$. Because the oscillators are identical, these are again overlapping.

Reentrainment involves choosing an initial condition in phase space and determining how long before the ensuing trajectory reaches and stays within a pre-chosen neighborhood of the LD-entrained solution. Eq. (2) represents a five-dimensional phase space, four for the independent variables and a fifth for the time variable. This is too large a phase space to study reentrainment, so we narrow down the study to something tractable. We first transform the time variable into the LD phase of light onset by performing a mod 24 operation. The phase will then be defined between 0 and 24, with 0 being the phase at which lights turn on, and then allowing phase to align with the hourly markings. Thus, in a 12:12 LD cycle, the lights turn on at phase 0 and turn off at phase 12. We choose a Poincaré section at $P_1 = 1.72$ and $0.15 \leq M_1 \leq 0.25$ which intersects the LD-entrained limit cycle of O_1. To study reentrainment, we fix O_1 at this intersection point, and allow O_2 to have an initial condition anywhere along its own LD-entrained limit cycle. Each point on that solution has a defined phase between 0 and 24. Thus, we restrict our study to consider initial conditions that have two different variations from the LD-entrained solution: a new phase of light onset and a new phase of O_2.

To assess entrainment, we place O_1 on the Poincaré section and O_2 anywhere along its own LD-entrained solution. We run the simulation until the return time for O_1 to its section falls within 12 min of 24 h. The entrainment time for O_1 is then defined as the sum of these return times. The criteria for O_2 is the same except that we add on the initial time it takes for the oscillator to cross the Poincaré section for the first time. The maximum of these two reentrainment times is then defined to be the total reentrainment time.

Fig. 3(a) shows two trajectories. The blue curve corresponds to O_1 which initially starts on the Poincaré section, completes one cycle and returns to the section. The associated first return time (≈22 h) is plotted in panel (b) with a blue dot. The orange curve is the trajectory of O_2 that begins at a location chosen along its LD entrained cycle. In Section 2.3, we explain how to relate an initial value of O_2 to a phase. Panel (a) shows two crossings of the section; the first has a short crossing time (referred to as the first return time in panel (b) with the lowest orange dot ≈4 h), and then a longer second return time of approximately 20 h. Note in panel (a) that while the second return location of O_2 to the Poincaré section appears to be close to that of O_1, these are occurring at different times and are thus not synchronized. Eventually the blue and orange dots converge to 24 h after enough returns and entrainment is declared.

2.3. Derivation of the entrainment map

In a series of prior papers [19,22,23], we have developed a tool called the entrainment map to facilitate finding the phase of entrainment of circadian oscillators with respect to the LD-cycle. In [19–21], we studied just a single oscillator forced by a 24-h LD signal, and constructed a one-dimensional entrainment map that measures the phase, denoted with the variable x, with respect to the onset of the lights of the circadian oscillator each time it crosses a Poincaré section. We showed that the map generally has two fixed points, a stable one, x_s, that corresponds to the LD-entrained solution and an unstable one, x_u, that, if the light intensity is low enough, corresponds to an unstable limit cycle (see [25] for details). Fig. 4(a) shows a schematic of the 1-dimensional entrainment map for a single oscillator. Fixed points occur when the map crosses the diagonal at $x_s = 4$ and $x_u = 15$. Their stability can be read off based on the slope at the crossing; stable (unstable) if the slope is less (greater) than 1 in magnitude. The map is periodic both on its top and right boundaries because of the mod 24 operation. Fig. 4(b–c) show a schematic of how the stable and unstable fixed points of the map translate to phases associated with limit cycles. The value $x = 0$ is where lights turn on and $x = 12$ is where they turn off. Oscillator 1 lies at the Poincaré section. The values x_s and x_u are the phase distances from $x = 0$ to the location of the Poincaré section. Note that since LD phase is measured when O_1 lies on its Poincaré section, the schematic circle rotates to place $x = 0$ in the appropriate location for the initial LD condition being considered. This is reflected in the different locations of red (lights on) and black (lights off) in panels (b) and (c).

In this paper, because we have two circadian oscillators, the entrainment map is two-dimensional. It is constructed using the Poincaré section, the initial LD phase, and the initial O_2 phase. Starting with O_1 on the Poincaré section, as above, let x equal the phase from when the lights last turned on and let y equal the phase of O_2 on its LD-entrained limit cycle; see Fig. 4(d). Note that unlike the location of $x = 0$, which changes depending on what initial LD phase is chosen, the location of $y = 0$ is always fixed since it is associated with the stable LD-entrained solution. Indeed, since the two oscillators are synchronized on the LD-entrained solution, $y = 0$ always lies a distance x_s before the Poincaré

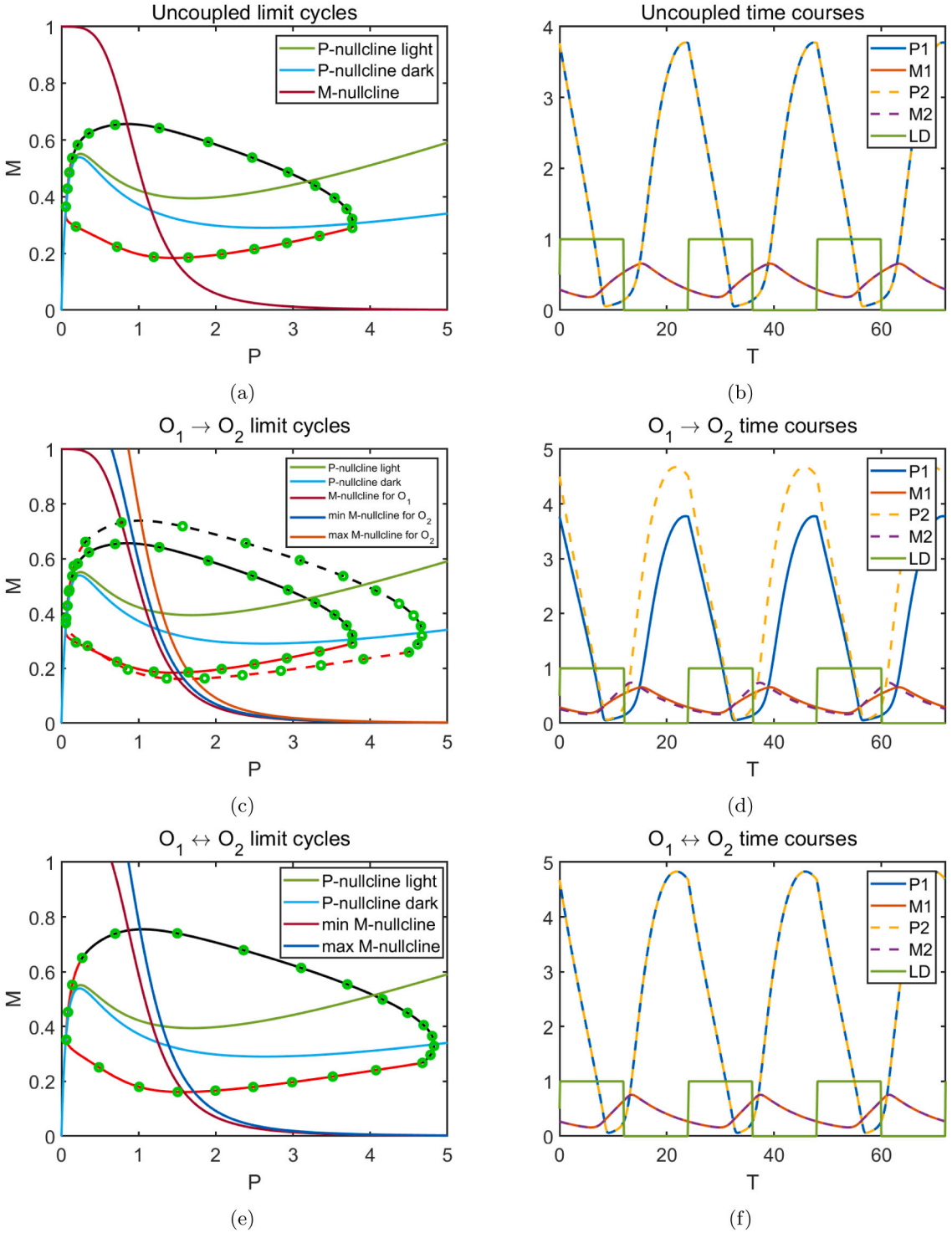

Fig. 2. Entrained solutions: phase space and time courses. (a) The dynamics of the uncoupled 24-h entrained system, in which the limit cycles of O_1 and O_2 are identical and overlap. The red portion occurs when lights are on, and the black portion occurs when lights are off. Green circles represent hourly markings. The direction of flow is clockwise. (b) Overlapping time courses for both M and P variables. (c) The dynamics of the hierarchically coupled system, in which there is no coupling from O_2 to O_1. The O_2 limit cycle (dashed curve) has larger amplitude than the O_1 limit cycle (solid curve), but both are entrained to the 24-h LD forcing. (d) Time courses show the resultant larger amplitude of P_2 compared to P_1. (e) The dynamics of the fully coupled system, with overlapping limit cycles. (f) Time courses also overlap and have larger amplitude than in (b).

section. The schematic in Fig. 4(d) also shows that the value $|y - x_s|$ is the amount of phase-tumbled desynchronization.

To provide some intuition on how to interpret the variables x and y, we consider a jet lag scenario. Suppose $x = 0$ corresponds to 6 AM. Then, the stable fixed point $x_s = 4$ corresponds to 10 AM. In panel (b), since O_1 is at $x = 4$ and the LD cycle is 12:12, it will receive 8 more hours of light. Now consider panel (d), which shows an example of traveling across time zones. Here, O_1 is at $x = 6$, corresponding to 12 PM. This is equivalent to having traveled 2 time zones east, and O_1 will only receive 6 more hours of light due to the shift in the LD cycle. This

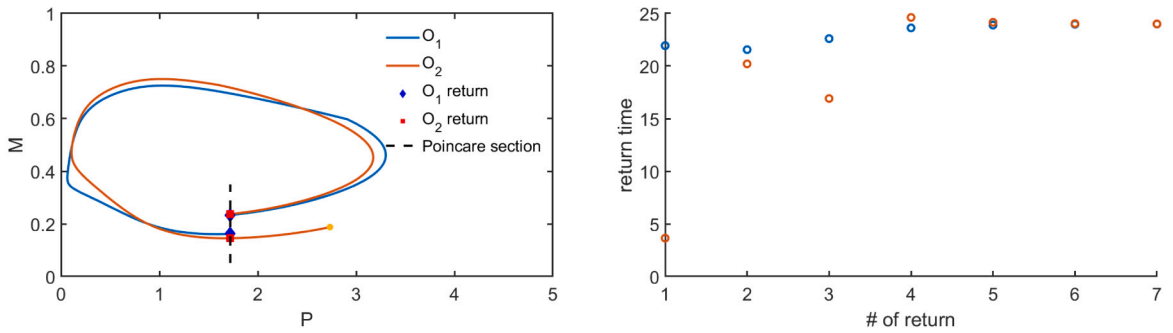

Fig. 3. Illustration and calculation of return times. (a) The Poincaré section and phase plane trajectories. The O_1 trajectory starts on the Poincaré section (lower blue diamond), moves clockwise, and terminates when it first returns to the section (upper blue diamond overlapped by upper red square). The O_2 trajectory starts on its own limit cycle at an arbitrary phase, and crosses the section twice (red squares). (b) Seven return times measuring the transit times are shown for when an oscillator's trajectory leaves the Poincaré section until it returns. The first O_2 return time is very short, consistent with (a). By the fifth return time, both oscillators are nearly entrained and take 24 h to return.

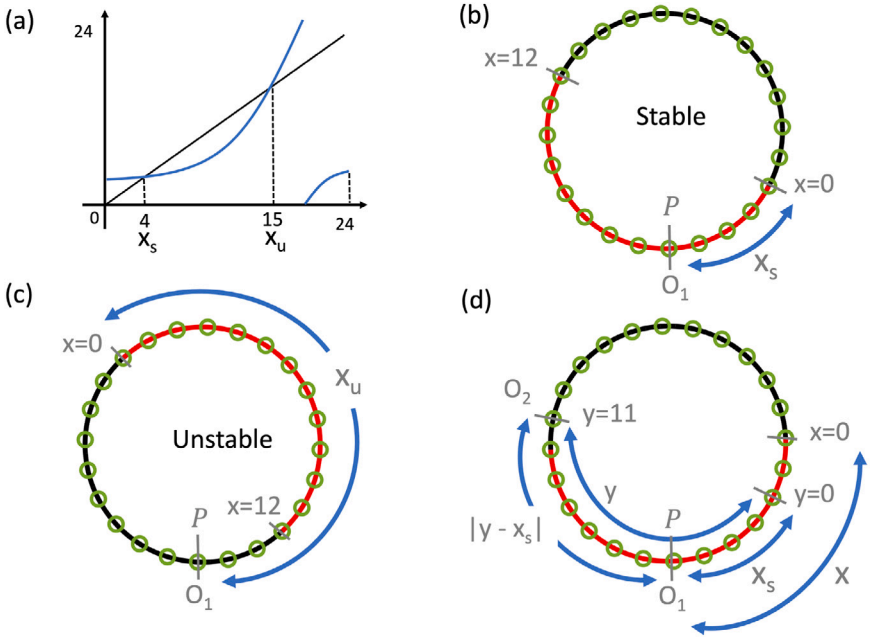

Fig. 4. Schematic identifying phases, initial conditions, and phase-tumbled desynchrony. (a) Typical one-dimensional entrainment map for a single oscillator. Intersection points with the diagonal correspond to stable ($x_s = 4$) and unstable ($x_u = 15$) fixed points. (b)–(d) O_1 always begins at the Poincaré section P (gray bar) located at the local minimum of the circle. Red (black) curves indicate hours when lights are on (off); green circles are hourly markings. Evolution along the phase circles is clockwise. (b) The stable configuration of phase ($x_s = 4$) for a single oscillator. Note that the Poincaré section is crossed four hours after the lights are turned on, as indicated by the blue arrow associated with x_s. (c) The unstable configuration of phase ($x_u = 15$) for a single oscillator. The phase circle is rotated relative to panel (b) such that the Poincaré section is crossed fifteen hours after the lights are turned on, as indicated by the blue arrow associated with x_u. (d) Phases of the coupled system for an arbitrary choice of LD and O_2 initial conditions. The location of $x = 0$ is chosen arbitrarily to lie on the phase circle, while the location of $y = 0$ is fixed to be x_s hours before the Poincaré section. The value $|y - x_s|$ is the initial phase-tumbled induced desynchrony that indicates how far O_2 has been shifted from the Poincaré section P.

is the only perturbation that O_1 receives. In contrast, O_2 will receive two perturbations: the 2-h shift in the LD cycle, as well as some amount of phase tumbling. First, let us consider the phase tumbling portion. In panel (d), the initial condition of O_2 has been perturbed (phase-tumbled) to $y = 11$. Thus, due to phase-tumbled induced desynchrony alone, O_2 is expecting to receive 1 more hour of light, as if it were 5 PM. This "fictive" arrival time would correspond to having traveled 7 time zones east, which is exactly $|y - x_s|$. However, due to the 2-h shift in the LD cycle, O_2 will actually receive 6 more hours of light, just like O_1. To summarize, therefore, the variable x can be interpreted as the arrival time of both O_1 and O_2 (12 PM). The variable y can be interpreted as the fictive arrival time due to phase tumbling without considering the shift in the LD cycle.

To calculate the map, we solve the set of Eqs. (2) from an initial value of (x, y) until O_1 returns to the Poincaré section. From there, by employing techniques we developed in Liao et al. [23], we determine the phase at which the lights last turned on and the current phase for O_2. Let $I = [0, 24]$. By following this procedure for all initial conditions $(x, y) \in I \times I$ we derive the entrainment map, which can be written:

$$x_{n+1} = F_1(x_n, y_n) \tag{3}$$

$$y_{n+1} = F_2(x_n, y_n). \tag{4}$$

Here the subscript n refers to the iterate of the map starting with the initial value $n = 0$. A fixed point of the map satisfies

$$x = F_1(x, y) \tag{5}$$

$$y = F_2(x, y). \tag{6}$$

The x-nullcline is the set of points that satisfy Eq. (5) and the y-nullcline is the set of point that satisfy Eq. (6). These nullclines can be found using a geometric method introduced in [23,26,27]. Namely consider the equations $z = x$ and $z = F_1(x, y)$. Both have domain $I \times I$ and are thus two-dimensional graphs. The intersection of these graphs in (x, y, z) space is a one-dimensional curve which is the x-nullcline.

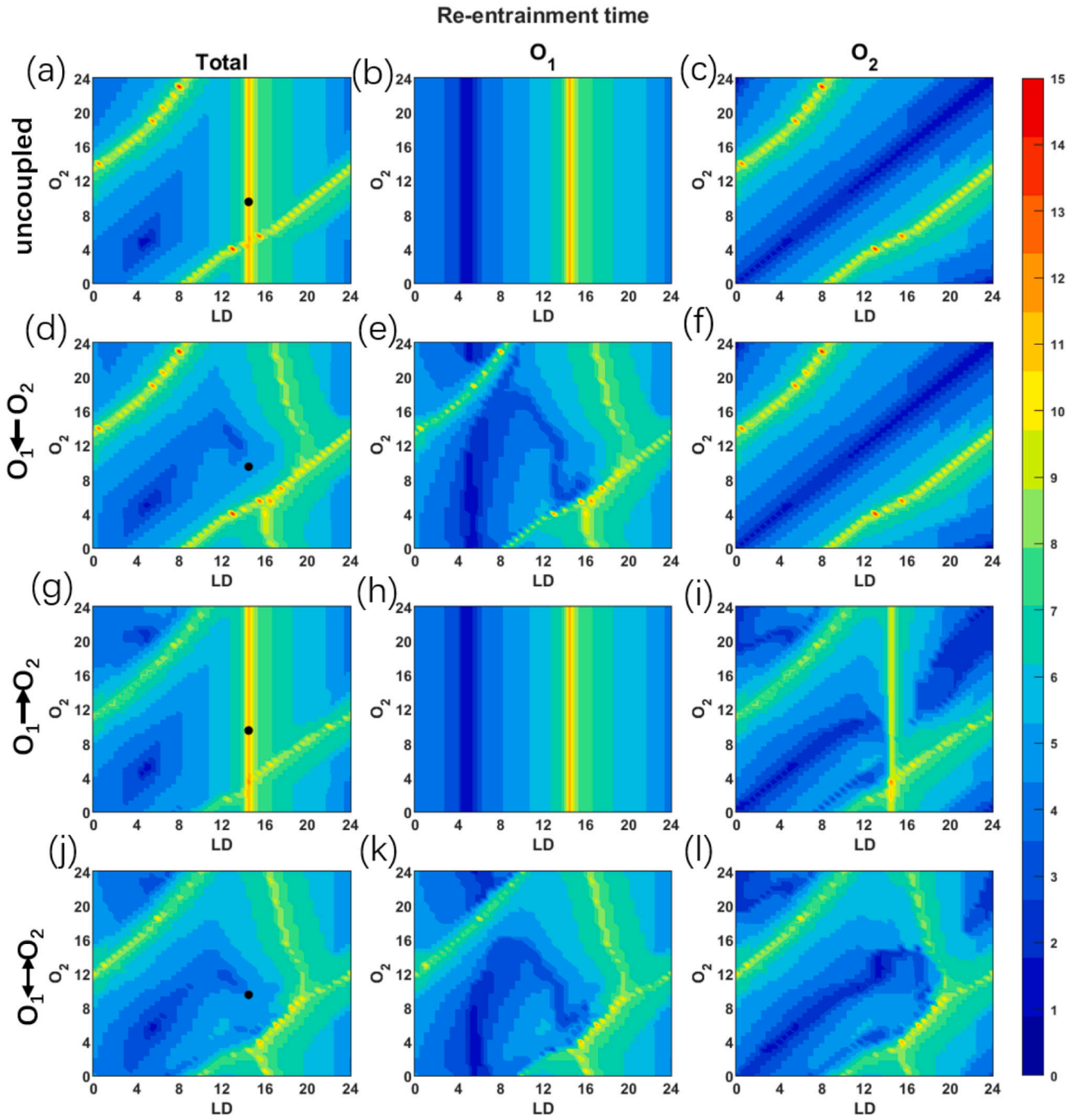

Fig. 5. Total reentrainment time for the four distinct coupling cases. The type of coupling is indicated on the left of each row. Total, O_1, and O_2 entrainment times (in days) are shown in columns 1, 2, and 3, respectively. Row 1: (a)–(c) The uncoupled case. It is straightforward to see how the heatmap in (a) follows by choosing the maximum time from (b) and (c). See text for a detailed description. Row 2: (d)–(f) The effect of coupling from O_2 into O_1. The long reentrainment time in (a) and (b) is destroyed by the coupling. Panels (c) and (f) are identical since O_2 does not receive any input from O_1. Row 3: (g)–(i) The effect of coupling from O_1 to O_2. Now panel (h) is identical to (b) since there is no new input to O_1. Alternatively, the coupling from O_1 to O_2 introduces some regions of faster reentrainment near the formerly very yellow bands, but more importantly, a new band of slow entrainment near $X = 14$. This band indicates that O_2 quickly synchronizes with O_1 and thus is slowed down in its reentrainment due to O_1. Row 4: (j)–(l) The fully coupled case. Note the similarity between panels (e) and (k). Also note that panel (l) has qualitatively the same shape since the reciprocal coupling has the effect of making the various entrainment times equalize. Column 1: The black dots represent the initial condition (14.5,9.5). Note how the different forms of coupling lead to different entrainment times.

Similarly we find the y-nullcline. The intersection of the projection of these nullclines onto $I \times I$ space corresponds to fixed points of the map. As we will show in the Results section, for the parameter sets of interest, the entrainment map has four fixed points. One of the fixed points is a stable node, two are unstable saddle points and the last is an unstable node. Understanding their stable and unstable manifolds will be critical for explaining the reentrainment results that we numerically obtain.

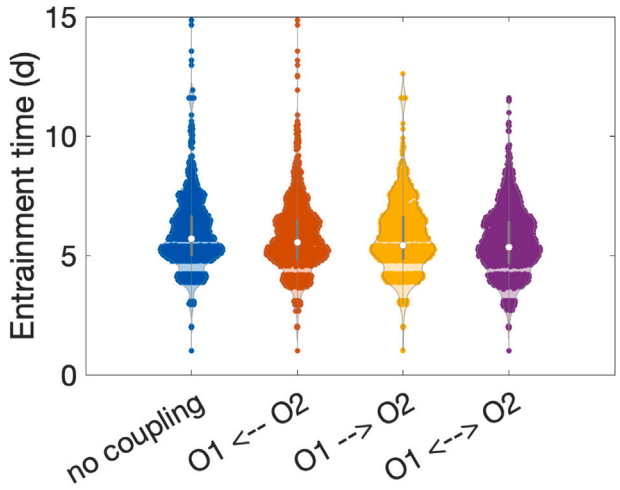

Fig. 6. Distributions of entrainment times. Violin plot showing the distribution of total entrainment times across all LD phases and initial O_2 phases with no coupling (blue), unidirectional coupling (orange and yellow), and bidirectional coupling (purple). The white dot is the median entrainment time for each case. The case of bidirectional coupling has the lowest reentrainment times on average, and in particular shows a reduction in the longest reentrainment times.

2.4. Numerical methods

Numerical simulations were performed in MATLAB (Mathworks Inc, Natick, MA). The `ode15s` solver was used to integrate the ODE systems. Computations associated with the entrainment map utilized methods described in [23]. Further details and code are provided in the following Github repository: https://github.com/daybrown/Phase-tumbling-project/.

3. Results

3.1. Reentrainment time analysis

Fig. 5 displays a heat map for the three types of re-entrainment time under the four different coupling possibilities. The first column depicts the total reentrainment time, and the second and third columns show the reentrainment times for O_1 and O_2, respectively (defined in the Methods section). The four rows consider each of the four different coupling scenarios. The LD phase is plotted on the horizontal axis, and the phase of O_2 is plotted on the vertical axis. Examining the uncoupled case shown in the first row, panel (b) shows that the phase of O_2 has no impact on the reentrainment time of O_1, evidenced by the invariance of the heat map in the vertical direction. Also note the vertical dark blue and red lines. These lines occur at phases at which O_1 is at the stable ($x_s = 5.635$) and unstable ($x_u = 14.5$) fixed points of the one-dimensional entrainment map, respectively. Similarly, panel (c) shows the dark blue (fast) and yellow (slow) reentrainment times for O_2. Note that the diagonal in this figure represents situations in which O_2 is placed at an initial condition y that is exactly matches the shift of the LD phase x; in other words O_2 starts entrained to the LD-cycle and remains so. Note that panel (c) does not display the same type of invariance as (b) because there is a qualitative difference between the initial conditions of O_1 and O_2. For O_1, the initial condition always lies on the Poincaré section, while for O_2, the initial value denotes a point on its LD-entrained solution and not necessarily on the section. The maximum times from panels (b) and (c) at each (x, y) are then used to compute the total reentrainment time in panel (a). Considering row 2, coupling from O_2 to O_1 does not change the reentrainment time for O_2; note panels (c) and (f) are identical. It does quite dramatically change O_1 reentrainment time as shown in panel (e), by on one hand shortening the long entrainment times near O_1's unstable fixed point (red line from (b) destroyed), and on the other hand, lengthening the entrainment time near its stable fixed point (blue line from (b) destroyed). Both make sense since the coupling will initially move O_1 away from a neighborhood of its stable and unstable phase. Row 3 shows that the coupling from O_1 to O_2 has similar effects, noting the differences in panels (c) and (i) and the lack of change from (b) to (h). For the fully coupled case shown in row 4, the different areas of slow entrainment (yellow curves) are now attributable to both O_1 and O_2, but in different ways. The primary effect of O_2 coupling onto O_1 is to shorten the O_1 reentrainment times (note the darker yellow in panel (e) has been replaced by lighter yellow or green in panel (k)).

There are several other features of these heat maps that we wish to highlight. In panels (a), (b), (g) and (h), the red vertical line at $x = 14.5$ passes through the unstable fixed point associated with O_1's one-dimensional entrainment map. In this two-dimensional setting, the red line represents the stable manifold of what we will show is an unstable saddle fixed point of a two-dimensional map that lies on that line (see Section 3.2). Initial data that lie close to this manifold will initially pass close to the unstable fixed point, and be trapped there for a large amount of time, before eventually converging to the stable LD-entrained solution. This is why the initial conditions on the red vertical line take so long to entrain. In panel (a), we also observe two yellow bands. Initial conditions in these bands also have long entrainment times. The band that intersects the red vertical line suggests that there may be an invariant structure at the intersection point and that the invariant manifold of that structure lies within the yellow band (this will also be discussed in Section 3.2). Note that when this yellow band hits either the lower or right boundary, because of periodicity it emerges from the upper or left boundaries, respectively. This suggests that there is also an invariant structure lying within the upper left yellow band. Moving down the first column, note the change or the consistency of these red and yellow bands as the different directions of coupling are introduced. Importantly, the yellow bands persist indicating that invariant structures persist in the coupled system. Qualitatively, while panels (d) and (j) look quite similar, indicating that the coupling from O_2 to O_1 plays a more critical role in the reentrainment process than coupling from O_1 to O_2, this is not an accurate conclusion. The fully coupled network is symmetric so there really is no difference between O_1 and O_2. The reason that the effects appear to be different has to do with the placement of the Poincaré section and the requirement that time measurements are made when O_1 lies on the section. In each panel of the first column appears a black dot at $x = 14.5$ and $y = 9.5$. This point is chosen to illustrate how the different forms of coupling affect reentrainment time for the same initial condition. Note that in panel (a) and (g), the black dot lies in the red band indicating long reentrainment, which from panel (h) can clearly be attributed to a long reentrainment time for O_1. Alternatively, in panels (d) and (j), the invariant structures (yellow bands) do not contain the black dot, thereby leading to faster reentrainment.

To assess the overall impact that coupling between oscillators has on their reentrainment, we used violin plots to compare the distributions of total reentrainment times for simulations with no coupling, unidirectional coupling, and bidirectional coupling across all LD and O_2 initial phases (Fig. 6). On average, coupling speeds up the entrainment process: the median reentrainment time is 5.7 days with no coupling, 5.6 days with $O_1 \leftarrow O_2$ coupling, 5.4 days with $O_1 \rightarrow O_2$ coupling, and 5.3 days with $O_1 \leftrightarrow O_2$ coupling. Certain types of coupling can also help reduce the length of reentrainment encountered in the worst-case scenarios: the longest reentrainment time is 14.9 days with either no coupling or $O_1 \leftarrow O_2$ coupling, 12.6 days with $O_1 \rightarrow O_2$, and 11.6 days with $O_1 \leftrightarrow O_2$ coupling. Note that there is an asymmetry between the $O_1 \leftarrow O_2$ and $O_2 \leftarrow O_1$ cases. This arises because the initial location of O_1 is always on the Poincaré section, whereas the initial location for O_2 can be anywhere along its own LD-entrained limit cycle. Swapping the coupling therefore will have different effects on reentrainment.

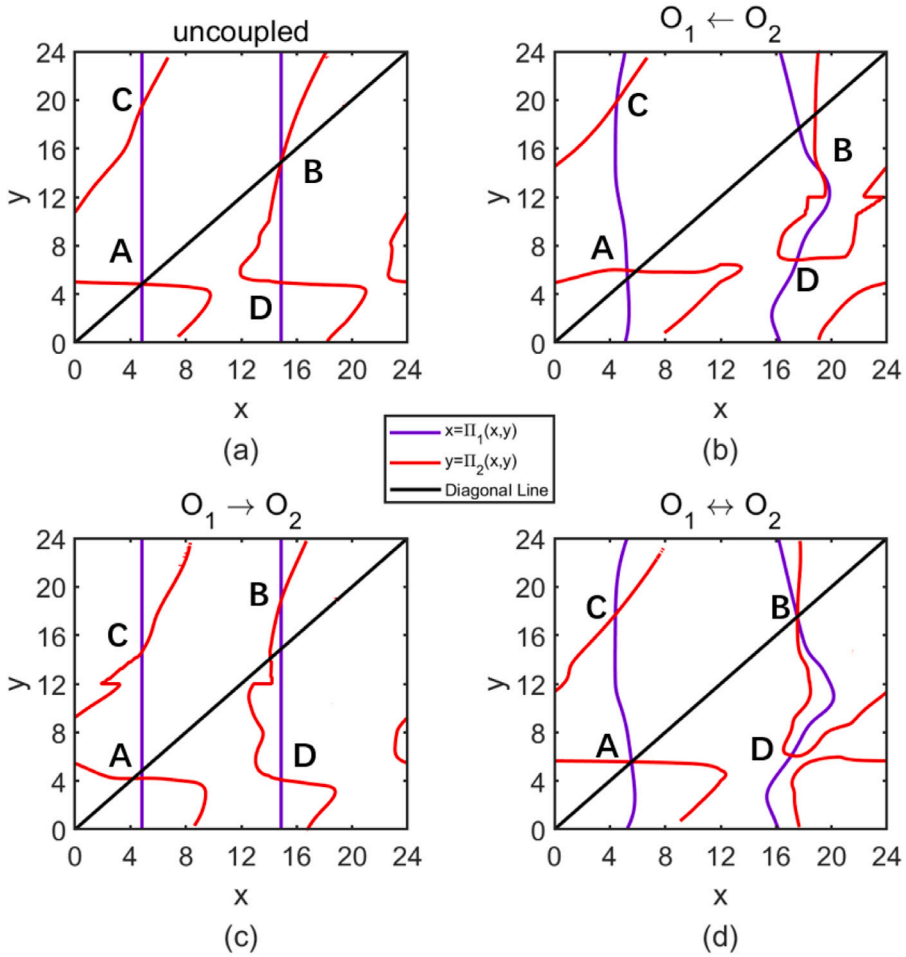

Fig. 7. Nullclines of the entrainment maps for the four types of coupling. Intersection of the nullclines corresponds to fixed points of the map. In each panel, the fixed point A is a stable node, B and C are saddles, and D is an unstable node. (a) The x-nullclines are vertical, since the oscillators are uncoupled. Fixed points A and B lie on the diagonal, indicating that the oscillators are synchronized. (b)–(c) When the coupling is not symmetric, the entrained solutions of the oscillators are not in phase. There is a phase difference between the oscillators leading to points A and B lying off of the diagonal. Note the changes to the x- and y-nulclines in (b) and just the y-nullclines in (c). This has to do with the choice of using O_1 as the reference oscillator for the Poincaré section. (d) Nullclines of the fully coupled system where fixed points A and B again lie on the diagonal indicating in-phase synchronization.

3.2. The two-dimensional entrainment map

In the previous section, we suggested that the red and yellow bands were signs of invariance. Here we more explicitly address this claim and explain how long entrainment times can arise. Consider the two dimensional map defined by Eqs. (3) and (4). In the Methods section we described how to find the x and y nullclines associated with this map, namely the set of points that satisfy Eqs. (5) and (6). By plotting these nullclines in the $x-y$ phase space of the map, we find points of intersection which correspond to fixed points of the map. In Fig. 7, we have plotted nullclines for the four different cases of coupling. In each panel, there are four intersection points. Given this is a two dimensional map, then sum of the dimensions of the stable, unstable and center manifolds of each of these fixed points must be two. To understand the nature of these fixed points, we first discuss panel (a) for the uncoupled case. In the uncoupled case, both Oscillator 1 and 2 have stable and unstable points independent of the other oscillator. Point A at $(x, y) = (5.635, 5.635)$ is where both O_1 and O_2 are at their stable fixed points with regard to their own one-dimensional maps. Thus this point has a two-dimensional stable manifold. Note that for the uncoupled case, point A must lie on the diagonal since the oscillators are identical and thus have the same value for the stable fixed points. An initial condition corresponding to point A is, by definition, entrained to the LD-cycle. Point B is where O_1 is at its unstable fixed point, but O_2 is at its stable fixed point. Thus, B is a saddle point, with a one-dimensional stable manifold and one-dimensional unstable manifold. Point C is the same, except the stability of O_1 and O_2 is reversed. Point D is where both lie at the unstable fixed points of their one-dimensional maps. Thus, point D has a two-dimensional unstable manifold. Therefore, the vertical red band in Fig. 5(a) is actually the stable manifold of the saddle point B which emanates as a part of the unstable manifold of point D. It is now easy to understand the yellow diagonal band near the bottom right and top left portions of Fig. 5(a). These are the one-dimensional stable manifolds of the saddle point at C that emanate from the unstable node point D. Finally, that point A corresponds to the stable node of the map explains why the region of Fig. 5(a) near $x = 5$ and $y = 5$ has the shortest entrainment time. The fixed points of panels (b), (c) and (d) of Fig. 7 have the same stability characteristics as those in panel (a). Note that the location of the fixed points moves but stays in a neighborhood of the locations of panel (a).

In Fig. 8(a), we re-plot the heat map of the fully coupled case, but now overlay the fixed points of the map obtained from the intersection of the nullclines. Points B, C and D all lie within the yellow slow entrainment bands. For the saddle points B and C, these are the one-dimensional stable manifolds, that coincide with the strong and weak unstable manifolds of the unstable node point D. The heat map does not reveal, however, the unstable manifolds of the saddle points, nor the stable manifolds of point A. To get a better sense of those, we plot

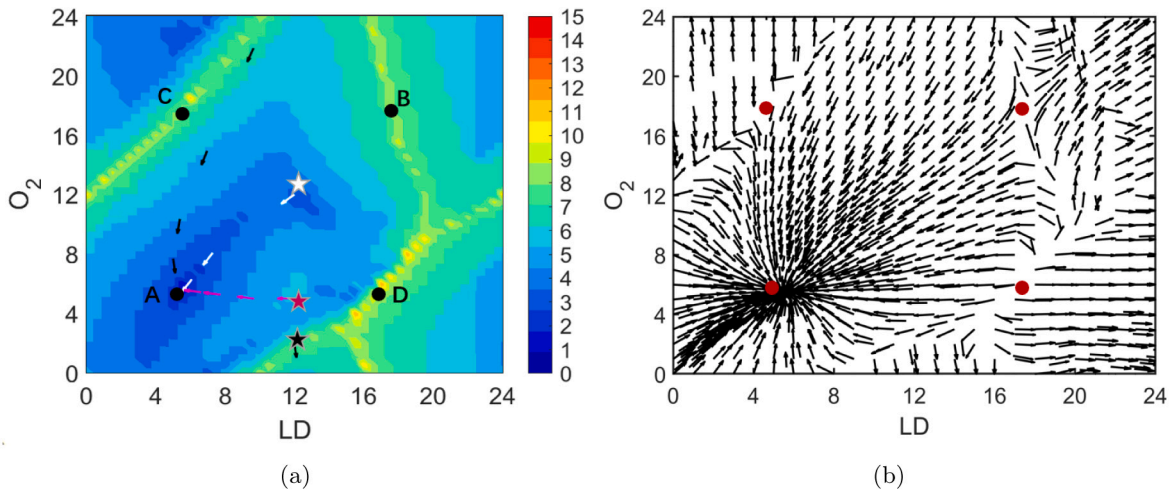

Fig. 8. Dynamics of entrainment map. (a) Heatmap of the fully coupled case. The four black dots are the fixed points of the corresponding 2D map. The white arrows are map iterations starting from the white star (12,12), the magenta arrows are map iterations starting from the red star (12,5), and the black arrows are map iterations starting from the black star (12,2). (b) Iterations of the map. Arrows indicate the direction of the next iterate. The saddle-like structure of points B and C (upper two red dots) can be discerned. Attraction to the stable node A (lower left red dot) occurs strongly along the diagonal.

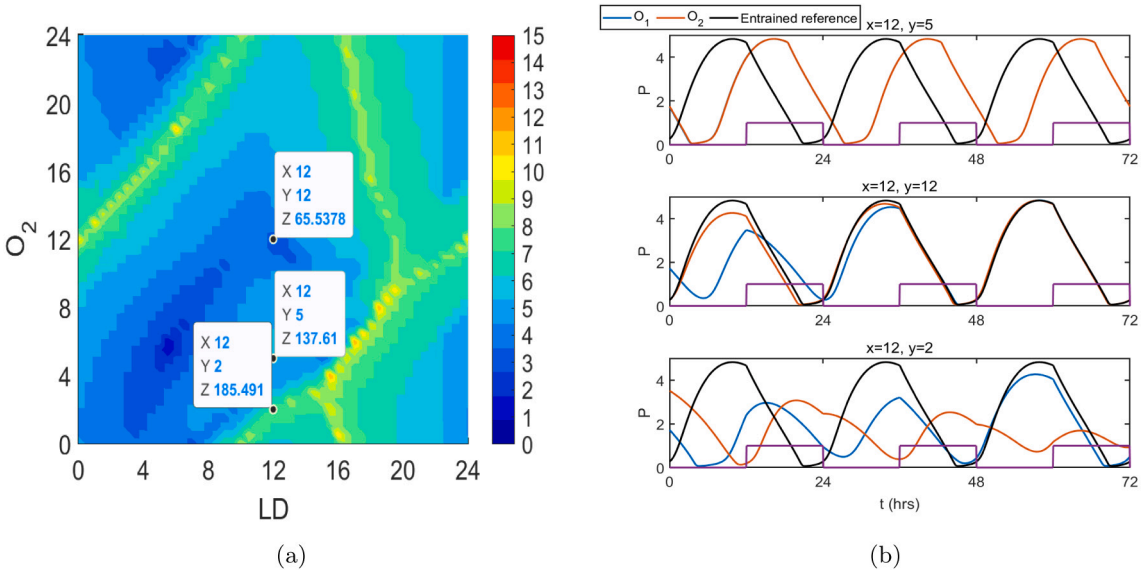

Fig. 9. Reentrainment time for three specific initial phases. (a) For the same LD phase $x = 12$, perturbing the phase of O_2 can either increase or decrease the reentrainment time. (b) The beginning portion of the time courses for reentrainment starting from three distinct initial conditions. The black time course is the entrained solution and serves as a reference. It is clear that when increasing $y = 5$ to $y = 12$, the reentrainment process is faster, while decreasing $y = 5$ to $y = 2$ slows down the reentrainment process.

in Fig. 8(b) the vector field of the map while overlaying in red dots the fixed points. From this figure, the unstable directions of points B and C are clearly evident and it is also clear that a large set of iterates, but not all, approach the stable fixed point along the diagonal. Looking again at panel (a), we plot the set of iterates starting at three distinct initial conditions $(12, 2)$ (black), $(12, 5)$ (red) and $(12, 12)$ (white) to show how they approach the stable node A. The black iterates, starting in a yellow band of long entrainment, follow the stable manifold of C (through the bottom of the graph to the top by periodicity) before eventually tracking the unstable manifold of C towards point A. The red iterates starting at $y = 5$, march into A horizontally indicating that O_1 and O_2 remain synchronized as they both entrain. Finally, the white iterates start on the diagonal for which O_2 is already in the correct phase alignment with LD. These iterates move towards point A along the diagonal indicating that O_2 maintains its phase alignment as O_1 entrains.

3.3. Phase tumbling

In this subsection, we study the effect of phase tumbling the oscillators prior to beginning the reentrainment process after a shift in phase of the light dark cycle. Recall that phase tumbling refers to the amount of desynchronization of the phases of O_1 and O_2 at the moment that they receive a change of the LD phase. In particular, since O_1 is always kept at the Poincaré section, a desynchronization is achieved by changing the initial location of O_2 along its limit cycle as measured by y. Phase-tumbled desynchrony is then defined to be $|y - x_s|$, where, in this case, $x_s = 5.635$. A key take away from this section is that phase tumbling does not always lead to faster entrainment. In fact, it depends quite critically on the change of LD phase as well as the specific value of the tumbled phase.

In the following, we focus on the fully coupled system. Fig. 9(a) is a duplication of Figs. 5(j) and 8(a). At LD phase $x = 12$, we have plotted the three different reentrainment times associated with $y = 2$, 5 and 12. As can be seen both from the time course shown in panel (b) and from

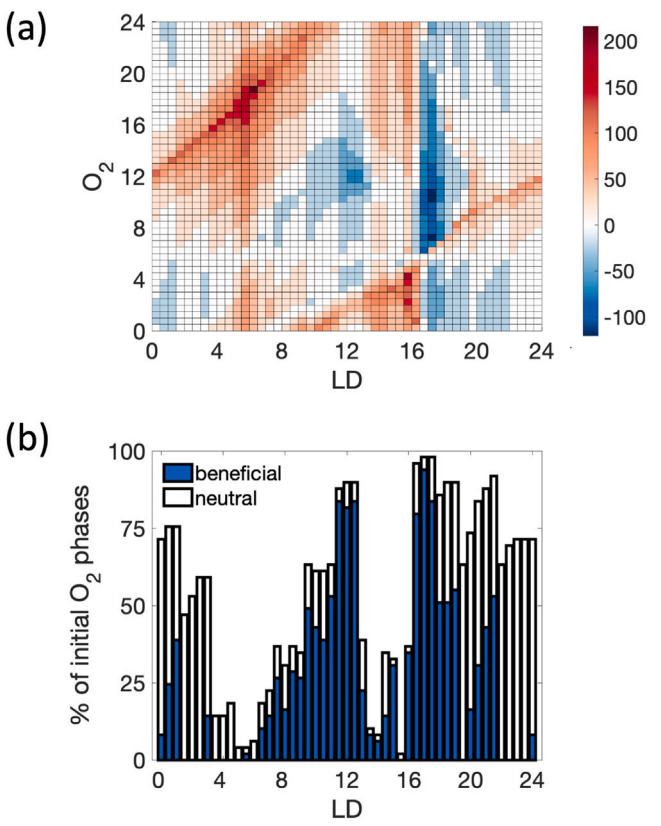

Fig. 10. Comparing phase-tumbled and synchronized reentrainment times. In all panels, we computed the difference in reentrainment time after an LD shift between $y = 5.635$ (O_1 and O_2 remain synchronized) and other initial phases that have been tumbled. (a) Colorbar indicates how many fewer hours or how many more hours it takes phase-tumbled initial conditions to reentrain than it does synchronized initial conditions. Blue colors (negative values) indicate faster reentrainment due to phase tumbling, i.e. where phase tumbling is beneficial. Red colors (positive values) indicate phase-tumbled initial conditions that are slower to reentrain, i.e. where phase tumbling is detrimental. White (a value of 0) indicates that the reentrainment time was the same for phase-tumbled and synchronized initial conditions, i.e. where phase tumbling is neutral. (b) For each LD phase, we compute the percentage of beneficial and neutral initial conditions. The advantage of phase tumbling is most pronounced in a neighborhood of $x = 17$, due to moving initial conditions away from the unstable node that exists for the synchronized solution at $y = 5.635$.

the total reentrainment time values, phase tumbling helps for the $y = 12$ case, but hurts for the $y = 2$ case. The explanation is straightforward. Any initial condition that lies in a neighborhood of a stable manifold of an unstable saddle point will take longer to reentrain since it will track the stable manifold to a neighborhood of the saddle point before iterating away towards the stable node. The initial value at $y = 2$ lies near the stable manifold of saddle point D. Alternatively, when $y = 12$, O_2 is at a location of phase space where it would naturally have been it were actually entrained to the LD cycle (since $x = 12$). This initial condition leads to the fastest entrainment. Thus in the case of $y = 2$, phase tumbling leads to longer reentrainment, and the case $y = 12$ leads to faster reentrainment relative to the case where O_1 and O_2 are minimally phase tumbled and remain nearly synchronized ($y = 5$).

To quantify this across a range of initial values in $x - y$ space, consider Fig. 10. In panel (a), at each vertical slice we computed the time difference for reentrainment starting at $y = 5$, which is close to the synchronized initial condition of 5.635, compared to the reentrainment time for phase tumbled initial conditions. Negative values (blue portions) indicate the degree to which phase tumbling is beneficial to speeding up reentrainment, and positive values (red portions) are the opposite. Not surprisingly the worst cases fall along the invariant manifolds of points B, C and D from Fig. 8. The figure gives a clear indication of regions where phase tumbling is expected to be beneficial, neutral or detrimental. Panel (b) plots the percent of O_2 initial phases along each vertical stripe of panel (a) for which phase tumbling is beneficial (blue) or neutral (white). Several conclusions can be drawn from panel (b). For small LD phase shifts near the stable phase of $x = 5$, phase tumbling is not beneficial. This occurs because when the phase shift is small, it makes little sense to desynchronize the oscillators and place one of them far away from the entrained solution. For larger phase shifts, namely near LD phases $x = 17$, almost all phase tumbling is beneficial. The reason is that at $x = 17$ the unstable node D (Fig. 8(a)) lies within the slow entrainment yellow band. So any phase tumbling that moves the initial condition outside of the yellow banded regions will be beneficial. Taking a vertical slice at $x = 17$, one observes that most, but not all, initial conditions lie outside of a yellow band so phase tumbling will be helpful in those cases. For LD phases near $x = 19$, phase tumbling is surprisingly detrimental. This is because the stable manifold of saddle point B is almost vertical in a vertical tubular neighborhood of that value. Thus, any phase tumbling would likely cause the initial condition to lie in a yellow banded slow entrainment region. Finally, as can be seen from the blue bars in panel (b), for almost all LD phases, there do exist initial values at which phase tumbling is beneficial. However, the tumbling has to be to a specific set of phases as documented in panel (a). Taken on average, the percentage of initial conditions for which phase tumbling is beneficial is 27.0%, while those for which phase tumbling is neutral is 27.4%. Thus, phase tumbling of initial conditions will be detrimental about 45% of the time, highlighting the need to be cautious when using phase tumbling as a strategy for reducing entrainment time.

3.4. Generalization with more than 2 oscillators

Having extensively explored the case of two oscillators, let us use the insights gained to extend our findings to the multi-oscillator case. However, extending this understanding to scenarios involving more than two oscillators presents new challenges as the increase in the number of possible interactions and pairwise combinations grows rapidly with each additional oscillator. As a result the general N oscillator case is too difficult to geometrically visualize using the entrainment map, though we have addressed the dynamics of this case using a simpler Kuramoto model in other work [22]. Instead, here we focus on the extension to three oscillators where we can use the previous sections results to qualitatively predict and understand some of the ensuing dynamics. Consider the following equations:

$$\begin{aligned}
\frac{dP_1}{dt} &= \nu_p M_1 - k_f h\left(P_1\right) - k_D P_1 - k_{L_1} f(t) P_1 \\
\frac{dM_1}{dt} &= \nu_m g(P_1) - k_m M_1 + (\alpha_{21} M_2 + \alpha_{31} M_3) g(P_1) \\
\frac{dP_2}{dt} &= \nu_p M_2 - k_f h\left(P_2\right) - k_D P_2 - k_{L_2} f(t) P_2 \\
\frac{dM_2}{dt} &= \nu_m g(P_2) - k_m M_2 + (\alpha_{12} M_1 + \alpha_{32} M_3) g(P_2) \\
\frac{dP_3}{dt} &= \nu_p M_3 - k_f h\left(P_3\right) - k_D P_3 - k_{L_3} f(t) P_3 \\
\frac{dM_3}{dt} &= \nu_m g(P_3) - k_m M_3 + (\alpha_{13} M_1 + \alpha_{23} M_2) g(P_3).
\end{aligned} \tag{7}$$

In this model, all oscillators receive LD forcing of the same strength ($k_{L_1} = k_{L_2} = k_{L_3} = 0.105$). The oscillators are all-to-all coupled with a common strength given by $\alpha_{ij} = 0.04725$. The rest of the parameters have the same meaning as the two-oscillator model.

Generalizing the methods of the previous section to the three oscillator case would require defining a three-dimensional map in which we would set a Poincaré section on the first oscillator, for example, and then have to track the three free phases, LD, O_2 and O_3. Such a map would be difficult to visualize and analyze. However, by studying specific situations, namely, by choosing specific LD phases to study, we

can reduce the problem back to a two-dimensional map. In doing so, we can understand the role of phase tumbling and make predictions of when phase tumbling will be beneficial, neutral or detrimental.

In Fig. 11, we select three particular LD phases. In panels (a) and (b), the LD phase is fixed at 12. By starting O_2 and O_3 near 12 too, fast reentrainment is observed because the latter two cells are already aligned to the LD phase. This is similar to our findings from Fig. 8(a). The yellow slow entrainment bands near the vertical line $O_2 = 2$ or the horizontal line $O_3 = 2$ exist because in the two oscillator case, the initial condition $(x, y) = (12, 2)$ was in a yellow band (see Fig. 8(a)). Since there is a symmetry with regard to O_2 and O_3, the heat map is also symmetric about the diagonal. In panel (b) we choose different O_2 phases and sample over the range of O_3 phases to show where long or fast reentrainment occurs. These results show that different initial O_2 phases lead to different sets of O_3 phases that lead to faster reentrainment. In panel (c) and (d), the LD phase is fixed at 5, where O_1 is near its stable entrained phase. Here regions that lie near the diagonal have fast entrainment with the exception of those that lie near the vertical $O_2 = 17$ or horizontal $O_3 = 17$ lines. These are the values at which the saddle point B and its stable manifold existed in Fig. 8(a). In panel (d) the local min near O_3 phase equal to 5 when the initial O_2 phase is also 5 makes sense since all oscillators are near the stable phase. The local maximum for each of the curves occurs near O_3 phase equal to 17 corresponding to the yellow regions of panel (c). Finally, in panels (e) and (f), the LD phase is fixed at 17, where O_1 is at its worst entrained phase. Not surprisingly, the slowest reentrainment occurs when O_2 and O_3 have initial conditions that are not near their aligned phase of $(17, 17)$. Instead, again using information from Fig. 8(a), note that point D lies at (17,5) and has very slow reentrainment. This means that the vertical and horizontal lines at $O_2 = 5$ and $O_3 = 5$ will have the longest reentrainment. In summary, we have used information from the two oscillator case of the previous section to determine, in specific cases, when faster or slower reentrainment for the three oscillator case should occur. In turn, these results further illustrate that phase tumbling, in and of itself, does not always lead to faster entrainment.

4. Discussion

Entrainment of the circadian cycle to the 24-h world is critical for the proper functioning of humans and other species. Beyond just entrainment, however, is correct alignment of the entrained phase to the 24-h light dark cycle. For humans, this can be measured, for example, through core body temperature, which shows a local minimum just before waking when properly aligned. The entrainment and alignment can be thrown off due to a variety of factors such as rapid travel across time zones (jet lag) or for workers who engage in shift work. In these circumstances, rapid reentrainment and realignment of the circadian rhythm is beneficial. The process of reentrainment is quite complicated and involves both reentrainment and synchronization of multiple oscillators in a single brain region (e.g. SCN) as well as across multiple different circadian systems organized in a hierarchical manner (e.g. peripheral oscillators [22,23,28,29]). Iterated maps representing ODE models of the circadian system can provide insights into entrainment dynamics [30,31].

In this paper, using a combination of simulations and analysis, we have concentrated on the case of a single region consisting of multiple oscillators to assess how to most quickly reentrain them after a change of LD phase. Past studies have suggested that desynchronizing these oscillators, phase tumbling, speeds up the reentrainment process. The results of this paper show that phase tumbling *may* be effective, but only in some situations that depends on the extent of both the LD phase shift as well as the specific amount of desynchronization achieved through phase tumbling. Using the two-dimensional entrainment map, we showed that for the two-oscillator case, there exist four possible entrained solutions. Only one of these is a stable solution. In particular, there exists an unstable entrained solution corresponding to a saddle point of the map in which the two oscillators are synchronized. When the LD phase shift places the synchronized oscillators in a neighborhood of this saddle point, reentrainment is quite long. Thus, any phase tumbling is beneficial as it moves the oscillators away from the stable manifold of the saddle point. On the contrary, for other LD shifts, phase tumbling may place an oscillator in the vicinity of a stable manifold of a saddle point. The iterates of the map then track this stable manifold to a neighborhood of the saddle point before eventually deviating. This causes long reentrainment times. Fig. 10 summarizes our findings across all phase shifts and phase tumbled initial conditions. As shown in the figure, almost 50% of phase tumbled initial conditions lead to *longer* reentrainment times than if the oscillators were to have remained synchronized. We further showed how our methods can be used to assess a network of three oscillators, though there are limitations in this extension as discussed later.

Throughout the paper we used a 12:12 LD duty cycle as well as a single intensity of light. There is no problem in extending to different LD duty cycles, however there are limitations in that entrainment is lost if there is too little light or dark within a given 24-h period. We have previously described how to handle changes in light intensity using multi-lux maps [21]. However the intensity of light does have non-intuitive effects on models of circadian oscillators. For example, as noted earlier, for one-dimensional entrainment maps at higher light intensities, the unstable fixed point need not correspond to an actual unstable periodic orbit; see [25]. Another non-intuitive finding is that for Kuramoto models [32], and likely one-dimensional phase models, fixed points can disappear through various bifurcations as light intensity increases [22]. We have not observed the loss of fixed points in models that utilize higher-dimensional circadian models. These mathematical curiosities remain to be better understood, along with any potential biological consequences.

Reentrainment is often studied using a phase response curve (PRC) which measures the change in phase of an oscillatory in response to a small perturbation. The PRC is constructed under the assumption that the perturbation keeps the oscillator in a neighborhood of its stable limit cycle. In the current study of phase tumbling, neither the desynchronizing inputs to the oscillators nor the change in LD phase can be considered perturbations. They are much larger and thus PRC methods are not well suited to address the questions that arise from it. Alternatively, the entrainment map [19] was developed specifically to handles all possible changes in LD phase across 24 h. The extension to consider two oscillators, first addressed in [23], also was undertaken to allow for changes of phase of the second oscillator across 24 h. In these studies it was the ability to identify fixed points of the map and the ensuing invariant manifold structure that allowed us in the current context to understand the effects of phase tumbling. However, the entrainment map does have some limitations. In particular, it is not well-suited to handle networks of large numbers of oscillators because the dimension of the entrainment map makes it untenable to calculate and analyze. There are other methods, such as considering a bank of phase oscillators in a continuum limit, that are capable of modeling such cases. Often, however, those models are not well connected to the underlying circadian biology. Another drawback of the entrainment map, that we have previously identified, is that the fixed points of the map do not necessarily correspond in a one-to-one manner with actual periodic solutions of the full set of equations (see [20] for further discussion of this point). However, Creaser et al. [25] performed a bifurcation analysis of a circadian oscillator model that demonstrated the existence of several phase space objects predicted by entrainment maps.

Mathematical findings and their significance to properties of circadian entrainment are related to previous findings of others [33,34] as well as some of our prior work [20,22,23]. For example, in their study of recovery from jet lag, Kori et al. [34] defines what they call a “jet lag separatrix”. They reduce their study to a one-dimensional phase model and this separatrix turns out to be an unstable fixed point of

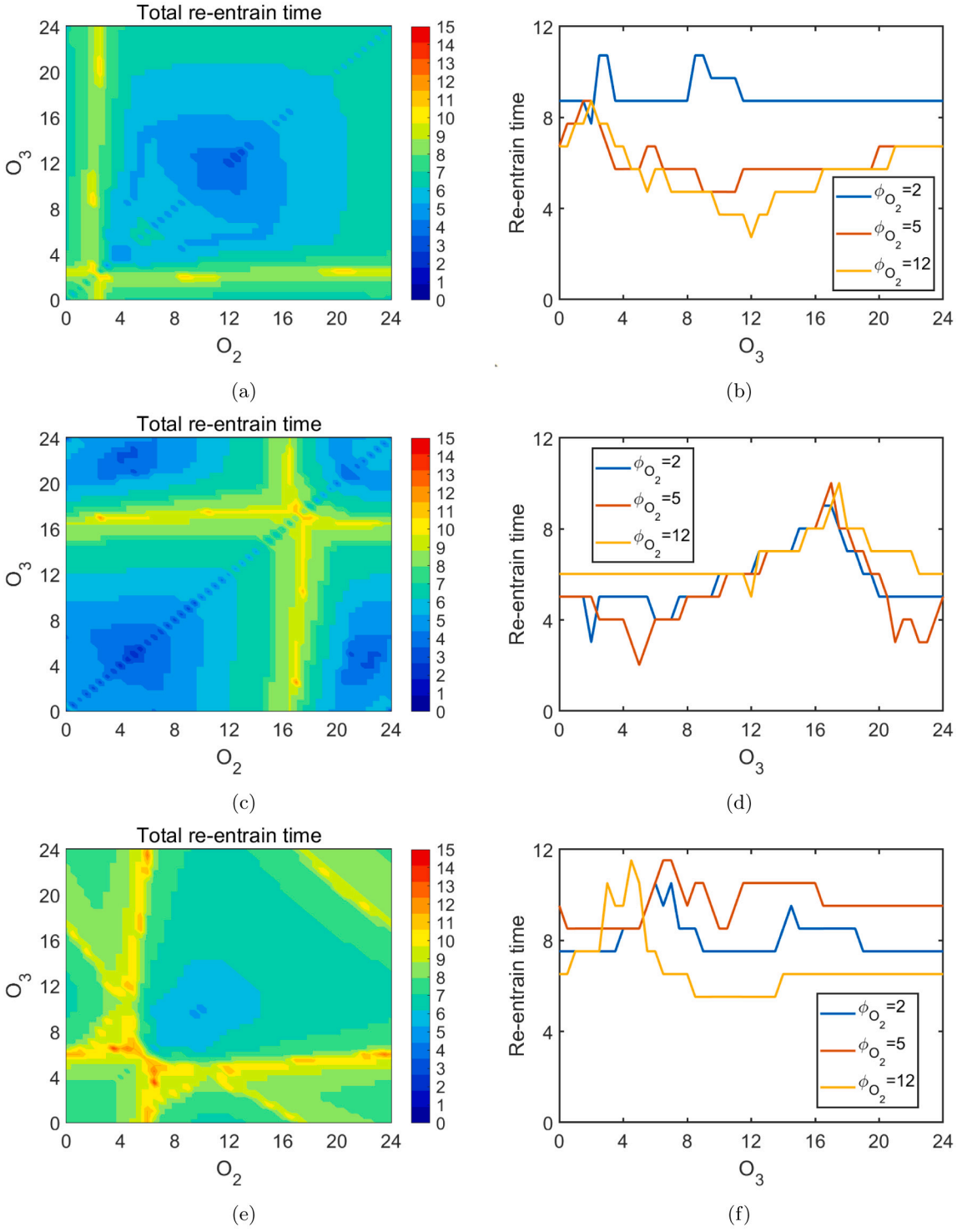

Fig. 11. Reentrainment times for distinct LD phases for the three-oscillator network. (a)–(b) The phase of LD is fixed at $x = 12$ as in Fig. 9. The phases of O_2 and O_3 are varied. Note that the yellow long reentrainment bands correspond to starting either O_2 or O_3 in a yellow band of Fig. 9(a) at $(12, 2)$. See text for a detailed description. Panel (b) shows how the reentrainment time varies with different initial O_3 phases for different values of initial O_2 phase. The local min (yellow curve) near O_3 at phase 12 is where O_2 and O_3 start at the entrained phase. (c) and (d) The phase of LD is fixed at 5, which is near the entrained phase. The total reentrainment time is faster near (5,5) and slower near (17,17). This, and the ensuing yellow, bands are consistent with either O_2 or O_3 lying near the stable manifold of a saddle point. Panel (d) shows a local min near $x = 5$ when O_2 also begins at 5, and a local max near $x = 17$, which is in vicinity of a stable manifold of a saddle point. (e)–(f) The phase of LD is fixed at 17, which is near the worst case of entrainment for the two-oscillator model. Slower entrainment occurs along both the initial phases $O_2 = 5$ and $O_3 = 5$, indicating that reentrainment is dictated by O_1. Panel (f) again shows that when O_2 and O_3 start at a phase that is entrained to the LD-phase shift of 12, fast reentrainment follows.

that model. Thus on the circle, it repels phase values sending them in opposite direction and thereby forms a separatrix of the phase space much in the same way that the saddle points of the entrainment map do. Lu et al. [33] also finds a similar phenomena in their study of jet lag. They use the Ott–Antonsen ansatz to derive a single complex equation of the order parameter. Since their equations are essentially two-dimensional, they find saddle, unstable and stable nodes much like ours.

There has been relatively little prior modeling work focused explicitly on the phase tumbling hypothesis. Roberts et al. [6] modeled the *Drosophila* circadian clock as a network of 60 coupled Goodwin oscillators [35]. They studied the dynamics of resynchronization following transient desynchrony in response to a phase-advancing light pulse, but did not simulate reentrainment to a phase-shifted light-dark cycle. An et al. [3] modeled the SCN as a network of 49 cells coupled through VIP signaling using a stochastic version of Leloup and Goldbeter's 16-dimensional model of circadian gene regulation [36]. They computed the phase response distribution (PRD) for pulses of VIP administered from Circadian Time (CT) 0 to CT24 (with CT0 defined as the minimum of *Period* gene expression). The PRD, which is similar to a PRC but displays the distribution of cellular responses rather than the aggregate response, showed the least phase dispersion near CT4 (the stable phase of entrainment) and the most phase dispersion at CT22. We speculate that CT4 corresponds to the stable fixed point of an entrainment map (point A in Fig. 7) and CT22 corresponds to the unstable node of an entrainment map (point D in Fig. 7). Simulations of their model with a pulse of light applied at CT19.5 and every 24 h thereafter converged to CT4 more quickly when initialized with desynchronized cellular phases (cells uniformly distributed between CT0 and CT24) than when initialized with synchronized cellular phases (all cells initialized at CT19.5). Based on their modeling results, the authors proposed the following strategy for minimizing jet lag: A traveler should arrive at their destination at a time when they would receive light exposure near CT22.

Our modeling study differs from An et al. [3] in that we simulated the entire range of possible phase advances and delays of the light-dark cycle due to travel (LD phase from 0 to 24) across the entire range of possible degrees of desynchronization for two oscillators (O_1 initial phase held constant and O_2 initial phase varied from 0 to 24). Our findings suggest that phase tumbling does not provide a guarantee of faster reentrainment, and, in fact, may lead to longer reentrainment times than if the oscillators remain synchronized.

Translating this to a direct application, we conclude that deliberately inducing phase tumbling after travel as a strategy for reducing jet lag would be inherently risky due to its potential to increase rather than decrease reentrainment times. However, there are certain LD phases for which phase tumbling is mostly beneficial or neutral. Thus, based on our modeling results, we propose the following strategy for reducing jet lag: A traveler should perturb (i.e. phase tumble) their clock upon arrival only if the LD phase in their destination time zone puts them in the neighborhood of the unstable node of the entrainment map. Future work is needed to determine how the location of the unstable node depends on network size, heterogeneity, and other parameters. Furthermore, employing this strategy requires knowledge of the traveler's circadian phase. While direct measurement of circadian phase is costly and impractical, indirect estimation using a combination of data from wearable devices and mathematical modeling can be quite accurate [37–39]. Other jet lag "pretreatment" strategies have been proposed [40–42], including a recent approach that exploits circadian memory (in the form of amplitude, rather than phase, coordinates) to hasten reentrainment [43]. Both experimental and modeling studies have shown that a stimulus of a certain strength applied at a certain phase can reduce the amplitude of a circadian oscillator to nearly zero and place the oscillator in a phaseless position referred to as the "singularity" [13,15,44–47]. Intentionally suppressing the amplitude of the oscillator upon arrival could shorten reentrainment time by allowing the trajectory to take a shortcut across phase space [20,25].

CRediT authorship contribution statement

Guangyuan Liao: Writing – review & editing, Writing – original draft, Visualization, Validation, Software, Methodology, Investigation, Funding acquisition, Formal analysis, Conceptualization. **Casey O. Diekman:** Writing – review & editing, Writing – original draft, Visualization, Validation, Software, Project administration, Methodology, Investigation, Funding acquisition, Formal analysis, Conceptualization. **Amitabha Bose:** Writing – review & editing, Writing – original draft, Visualization, Validation, Supervision, Project administration, Methodology, Investigation, Formal analysis, Conceptualization.

Declaration of competing interest

The authors have declared no conflict of interest

Acknowledgments

This paper is dedicated to Professors Martin Golubitsky and Avner Friedman, two former directors of the Mathematical Biosciences Institute at The Ohio State University, on the occasion of their retirement and in appreciation of their leadership and contributions to the dynamical systems and life sciences communities. GL: This work is supported by the Scientific Research Starting Foundation of Chongqing University of Posts and Telecommunications, China (Grant No. A2022-289), China Postdoctoral Science Foundation, China (Grant No. 2022M720549), and Chongqing Postdoctoral Innovation Talent Support Program, China (Grant No. CQBX202223). CD: This material is based on work partially supported by the National Science Foundation, United States under grant No. DMS-2152115. AB: This material is based upon work supported by the National Science Foundation, United States under Grant No. DMS-1929284 while the author was in residence at the Institute for Computational and Experimental Research in Mathematics in Providence, RI, during the Math + Neuroscience: Strengthening the Interplay Between Theory and Mathematics program.

Data availability

Code associated with this study is provided in the following Github repository: https://github.com/daybrown/Phase-tumbling-project/.

References

[1] T. Roenneberg, M. Merrow, The circadian clock and human health, Curr. Biol. 26 (10) (2016) R432–R443.
[2] A.M. Vosko, C.S. Colwell, A.Y. Avidan, Jet lag syndrome: circadian organization, pathophysiology, and management strategies, Nat. Sci. Sleep (2010) 187–198.
[3] S. An, R. Harang, K. Meeker, D. Granados-Fuentes, C.A. Tsai, C. Mazuski, J. Kim, F.J. Doyle III, L.R. Petzold, E.D. Herzog, A neuropeptide speeds circadian entrainment by reducing intercellular synchrony, Proc. Natl. Acad. Sci. 110 (46) (2013) E4355–E4361.
[4] C. Mazuski, E.D. Herzog, Circadian rhythms: To sync or not to sync, Curr. Biol. 25 (8) (2015) R337–R339, http://dx.doi.org/10.1016/j.cub.2015.02.032.
[5] L. Roberts, T.L. Leise, T. Noguchi, A.M. Galschiodt, J.H. Houl, D.K. Welsh, T.C. Holmes, Light evokes rapid circadian network oscillator desynchrony followed by gradual phase retuning of synchrony, Curr. Biol. 25 (2015) 858–867.
[6] L. Roberts, T.L. Leise, D.K. Welsh, T.C. Holmes, Functional contributions of strong and weak cellular oscillators to synchrony and light-shifted phase dynamics, J. Biol. Rhythms 31 (4) (2016) 337—-351.
[7] D.A. Golombek, R.E. Rosenstein, Physiology of circadian entrainment, Physiol. Rev. 90 (3) (2010) 1063–1102.
[8] A.M. Vosko, A. Schroeder, D.H. Loh, C.S. Colwell, Vasoactive intestinal peptide and the mammalian circadian system, Gen. Comp. Endocrinol. 152 (2–3) (2007) 165–175.
[9] U. Abraham, A.E. Granada, P.O. Westermark, M. Heine, A. Kramer, H. Herzel, Coupling governs entrainment range of circadian clocks, Mol. Syst. Biol. 6 (2010) 438.
[10] E. Buhr, S. Yoo, J. Takahashi, Temperature as a universal resetting cue for mammalian circadian oscillators, Science 330 (6002) (2010) 379–385.
[11] J. Enright, Temporal precision in circadian systems: A reliable neuronal clock from unreliable components? Science 209 (4464) (1980) 1542–1545.
[12] E. Herzog, J. Takahashi, G. Block, Clock controls circadian period in isolated suprachiasmatic nucleus neurons, Nat. Neurosci. 1 (8) (1998) 708–713.
[13] M. Jewett, R. Kronauer, C. Czeisler, Light-induced suppression of endogenous circadian amplitude in humans, Nature 350 (6313) (1991) 59–62.
[14] S. Pulivarthy, T. Nobushige, D.K. Welsh, L. De Haro, I.M. Verma, S. Panda, Reciprocity between phase shifts and amplitude changes in the mammalian circadian clock, Proc. Natl. Acad. Sci. USA 104 (51) (2007) 20356–20361.

[15] H. Ukai, T.J. Kobayashi, M. Nagano, K.-h. Masumoto, M. Sujino, T. Kondo, K. Yagita, Y. Shigeyoshi, H.R. Ueda, Melanopsin-dependent photo-perturbation reveals desynchronization underlying the singularity of mammalian circadian clocks, Nat. Cell Biol. (11) (2007) 1327–1334.
[16] M.H. Vitaterna, C.H. Ko, A.-M. Chang, E.D. Buhr, E.M. Fruechte, A. Schook, M.P. Antoch, F.W. Turek, J.S. Takahashi, The mouse clock mutation reduces circadian pacemaker amplitude and enhances efficacy of resetting stimuli and phase-response curve amplitude, Proc. Natl. Acad. Sci. USA 103 (24) (2006) 9327–9332.
[17] A. Winfree, Unclocklike behaviour of biological clocks, Nature 253 (5490) (1975) 315–319.
[18] J. Tyson, C. Hong, C. Thron, B. Novak, A simple model of circadian rhythms based on dimerization and proteolysis of PER and TIM, Biophys. J. 77 (1999) 2411–2417.
[19] C.O. Diekman, A. Bose, Entrainment maps: A new tool for understanding properties of circadian oscillator models, J. Biol. Rhythms 31 (6) (2016) 598–616.
[20] C.O. Diekman, A. Bose, Reentrainment of the circadian pacemaker during jet lag: East-west asymmetry and the effects of north-south travel, J. Theoret. Biol. 437 (2018) 261–285.
[21] C.O. Diekman, A. Bose, Beyond the limits of circadian entrainment: Non-24-h sleep-wake disorder, shift work, and social jet lag, J. Theoret. Biol. 545 (2022) 111148.
[22] G. Liao, A. Bose, Entrainment within hierarchical circadian oscillator networks, Math. Biosci. 351 (2022) 108883.
[23] G. Liao, C. Diekman, A. Bose, Entrainment dynamics of forced hierarchical circadian systems revealed by 2-dimensional maps, SIAM J. Appl. Dyn. Syst. 19 (3) (2020) http://dx.doi.org/10.1137/19M1307676.
[24] B. Novak, J. Tyson, Design principles of biochemical oscillators, Nat. Rev. Mol. Cell Biol. 9 (2008) 981–991.
[25] J.L. Creaser, C.O. Diekman, K.C. Wedgwood, Entrainment dynamics organised by global manifolds in a circadian pacemaker model, Front. Appl. Math. Stat. 7 (2021) 703359.
[26] Z. Akcay, A. Bose, F. Nadim, Effects of synaptic plasticity on phase and period locking in a network of two oscillatory neurons, J. Math. Neurosci. 4 (2014) 1–29.
[27] Z. Akcay, X. Huang, F. Nadim, A. Bose, Phase-locking and bistability in neuronal networks with synaptic depression, Phys. D: Nonlinear Phenom. 364 (2018) 8–21.
[28] N. Bagheri, S.R. Taylor, K. Meeker, L.R. Petzold, F.J. Doyle III, Synchrony and entrainment properties of robust circadian oscillators, J. R. Soc. Interface 5 (suppl_1) (2008) S17–S28.
[29] S.R. Taylor, A. Cheever, S.M. Harmon, Velocity response curves demonstrate the complexity of modeling entrainable clocks, J. Theoret. Biol. 363 (2014) 307–317.
[30] C. Athanasouli, S.H. Piltz, C.G. Diniz Behn, V. Booth, Bifurcations of sleep patterns due to homeostatic and circadian variation in a sleep-wake flip-flop model, SIAM J. Appl. Dyn. Syst. 21 (3) (2022) 1893–1929.
[31] G. Derks, P.A. Glendinning, A.C. Skeldon, Creation of discontinuities in circle maps, Proc. R. Soc. A 477 (2251) (2021) 20200872.
[32] Y. Kuramoto, Chemical Oscillations, Waves, and Turbulence, Springer Berlin, Heidelberg, 1984.
[33] Z. Lu, K. Klein-Cardena, S. Lee, T.M. Antonsen, M. Girvan, E. Ott, Resynchronization of circadian oscillators and the east-west asymmetry of jet-lag, Chaos: Interdiscip. J. Nonlinear Sci. 26 (9) (2016).
[34] H. Kori, Y. Yamaguchi, H. Okamura, Accelerating recovery from jet lag: prediction from a multi-oscillator model and its experimental confirmation in model animals, Sci. Rep. 7 (1) (2017) 46702.
[35] A. Woller, D. Gonze, T. Erneux, The goodwin model revisited: Hopf bifurcation, limit-cycle, and periodic entrainment, Phys. Biol. 11 (4) (2014) 045002.
[36] J.-C. Leloup, A. Goldbeter, Toward a detailed computational model for the mammalian circadian clock, Proc. Natl. Acad. Sci. 100 (12) (2003) 7051–7056.
[37] W.A. Hofstra, A.W. De Weerd, How to assess circadian rhythm in humans: a review of literature, Epilepsy Behav. 13 (3) (2008) 438–444.
[38] Y. Huang, C. Mayer, P. Cheng, A. Siddula, H.J. Burgess, C. Drake, C. Goldstein, O. Walch, D.B. Forger, Predicting circadian phase across populations: a comparison of mathematical models and wearable devices, Sleep 44 (10) (2021) zsab126.
[39] Y.M. Song, J. Jeong, A.A. de Los Reyes, D. Lim, C.-H. Cho, J.W. Yeom, T. Lee, J.-B. Lee, H.-J. Lee, J.K. Kim, Causal dynamics of sleep, circadian rhythm, and mood symptoms in patients with major depression and bipolar disorder: insights from longitudinal wearable device data, EBioMedicine 103 (2024).
[40] H.J. Burgess, S.J. Crowley, C.J. Gazda, L.F. Fogg, C.I. Eastman, Preflight adjustment to eastward travel: 3 days of advancing sleep with and without morning bright light, J. Biol. Rhythms 18 (4) (2003) 318–328.
[41] S. Deacon, J. Arendt, Adapting to phase shifts, I. An experimental model for jet lag and shift work, Physiol. Behav. 59 (4–5) (1996) 665–673.
[42] V.L. Revell, C.I. Eastman, How to trick mother nature into letting you fly around or stay up all night, J. Biol. Rhythms 20 (4) (2005) 353–365.
[43] T. Ahmed, D. Wilson, Exploiting circadian memory to hasten recovery from circadian misalignment, Chaos: Interdiscip. J. Nonlinear Sci. 31 (7) (2021).
[44] M. Sun, Y. Wang, X. Xu, L. Yang, Dynamical mechanism of circadian singularity behavior in neurospora, Phys. A 457 (2016) 101–108, http://dx.doi.org/10.1016/j.physa.2016.03.030, URL https://www.sciencedirect.com/science/article/pii/S0378437116300280.
[45] A.T. Winfree, Integrated view of resetting a circadian clock, J. Theoret. Biol. 28 (3) (1970) 327–374, http://dx.doi.org/10.1016/0022-5193(70)90075-5, URL https://www.sciencedirect.com/science/article/pii/0022519370900755.
[46] K. Serkh, D.B. Forger, Optimal schedules of light exposure for rapidly correcting circadian misalignment, PLoS Comput. Biol. 10 (4) (2014) 1–14, http://dx.doi.org/10.1371/journal.pcbi.1003523.
[47] A.T. Winfree, Resetting the human clock, Nature 350 (6313) (1991) 18, http://dx.doi.org/10.1038/350018a0.